

# Exciton dynamics in luminescent carbon nanodots: Electron–hole exchange interaction

Bo Peng<sup>1,†</sup> (✉), Xin Lu<sup>1</sup>, Shi Chen<sup>1</sup>, Cheng Hon Alfred Huan<sup>1</sup>, Qihua Xiong<sup>1,2</sup> (✉), Evren Mutlugun<sup>3</sup>, Hilmi Volkan Demir<sup>3</sup>, and Siu Fung Yu<sup>4</sup>

<sup>1</sup> Division of Physics and Applied Physics, School of Physical and Mathematical Sciences, Nanyang Technological University, Singapore 637371, Singapore

<sup>2</sup> NOVITAS, Nanoelectronics Centre of Excellence, School of Electrical and Electronic Engineering, Nanyang Technological University, Singapore 639798, Singapore

<sup>3</sup> LUMINOUS, Centre of Excellence for Semiconductor Lighting and Displays, School of Electrical and Electronic Engineering, Nanyang Technological University, Singapore 639798, Singapore

<sup>4</sup> Department of Applied Physics, the Hong Kong Polytechnic University, Hong Hum, Hong Kong SAR, China

<sup>†</sup> Present address: National Engineering Research Center of Electromagnetic Radiation Control Materials, University of Electronic Science and Technology of China, No.4, Block 2, North Jianshe Road, Chengdu 610054, China

Received: 22 July 2015

Revised: 29 October 2015

Accepted: 30 October 2015

© Tsinghua University Press and Springer-Verlag Berlin Heidelberg 2015

## KEYWORDS

carbon dots, photoluminescence, pyrolysis, electron–hole exchange interaction, energy splitting

## ABSTRACT

The electron–hole exchange interaction significantly influences the optical properties of excitons and radiative decay. However, exciton dynamics in luminescent carbon dots (Cdots) is still not clear. In this study, we have developed a simple and efficient one-step strategy to synthesize luminescent Cdots using the pyrolysis of oleylamine. The  $sp^2$  clusters of a few aromatic rings are responsible for the observed blue photoluminescence. The size of these clusters can be tuned by controlling the reaction time, and the energy gap between the  $\pi$ – $\pi^*$  states of the  $sp^2$  domains decreases as the  $sp^2$  cluster size increases. More importantly, the strong electron–hole exchange interaction results in the splitting of the exciton states of the  $sp^2$  clusters into the singlet-bright and triplet-dark states with an energy difference  $\Delta E$ , which decreases with increasing  $sp^2$  cluster size owing to the reduction of the confinement energy and the suppression of the electron–hole exchange interaction.

## 1 Introduction

As a new fascinating class of carbon nanomaterials, luminescent carbon dots (Cdots) have attracted sig-

nificant attention owing to their favorable properties of good biocompatibility, low toxicity, and low cost, which offer the opportunity to substitute highly toxic semiconductor quantum dots (like CdSe and CdTe)

Address correspondence to Qihua Xiong, [Qihua@ntu.edu.sg](mailto:Qihua@ntu.edu.sg); Bo Peng, [bo\\_peng@uestc.edu.cn](mailto:bo_peng@uestc.edu.cn)

in bio-imaging applications and light-emitting diodes (LEDs) [1–5]. After the development of an electrophoretic method to purify fluorescent carbon materials from arc-discharge soot [6], the past few years have witnessed considerable progress in developing physical and chemical preparation methods for Cdots. For instance, graphite has been cut into ultra-small luminescent Cdots using a laser ablation approach [7], electrochemical synthesis [8], and a hydrothermal cutting method [9]. Furthermore, the soot from burning candles or natural gas has been oxidized to synthesize Cdots [10, 11]. The pyrolysis approach has been employed using carbohydrates, citric acid, and ethylenediaminetetraacetic acid as carbon precursors [12–15]. Previous reports have demonstrated that carbon architectures show similar photoluminescence (PL) behavior, whether they are carbon nanotubes [16] or amorphous [17] and crystalline [18] carbon particles. Based on the study of luminescent Cdots fabricated by cutting graphite/graphene sheets, three main explanations have been proposed for the origin of PL: emissive surface defects [12, 17], localized electron–hole pairs from  $\pi$ – $\pi^*$  states in  $sp^2$  clusters [19], and zigzag sites with a carbene-like triplet ground state [9, 13]. However, the mechanism of exciton dynamics in Cdots has not yet been studied.

Herein, we demonstrate a simple one-step method for the synthesis of luminescent Cdots by the pyrolysis of oleylamine. This approach can be extended to other alkylamines and silanes. In the synthetic system, oleylamine is the only chemical, acting simultaneously as a solvent, a precursor, and a passivation agent. We synthesized different luminescent Cdots by controlling the reaction time and further investigated their exciton dynamics. Fourier-transform infrared (FTIR), Raman, nuclear magnetic resonance ( $^1\text{H}$ NMR) spectroscopy, and X-ray photoelectron spectroscopy (XPS) data confirmed that the alkylamines were oxidized into  $sp^2$  domains. Our experimental data demonstrated that the absorption and PL position of the Cdots were red-shifted owing to the decrease of the energy gap between the  $\pi$ – $\pi^*$  states of the  $sp^2$  domains as the reaction time increased, which resulted in an increasing  $sp^2$  cluster size. Furthermore, the exciton dynamics in Cdots showed that the electron–hole exchange interaction in the  $sp^2$  domains generated a large

splitting between optically active (singlet-bright) and optically passive (triplet-dark) electrons (electron–hole excitations). The electron–hole exchange interaction and confinement energy decreased with increasing  $sp^2$  cluster size.

## 2 Experimental

### 2.1 Synthesis of carbon dots

Photoluminescent Cdots were synthesized by the carbonization of one organic solvent. First, 8-mL glass vials were heated at 380 °C for 10 min and then 50  $\mu\text{L}$  oleylamine was quickly added to the vials. The reaction time was set at 1, 5, 10, 20, and 30 min. After cooling to room temperature, the obtained Cdots were directly dispersed in 4 mL hexane. 0.2 mL of Cdots dispersion solution were extracted and diluted by hexane to 2 mL for the absorption and PL measurements. Oleylamine can be substituted by other organic sources, such as octadecanethiol, dodecanethiol, hexadecyltrimethoxysilane (HDTMSi), hexadecylamine, dodecylamine, 3-aminopropyltrimethoxysilane (APTMS), and N-(2-Aminoethyl)-3-aminopropyltrimethoxysilane (AEPTMS).

### 2.2 Characterization

Transmission electron microscopy (TEM) investigations were performed using a JEOL1400 transmission electron microscope with an accelerating voltage of 100 kV. Ultraviolet–visual (UV–Vis) absorption spectra were recorded at room temperature using a Lambda 950 spectrophotometer. Room-temperature steady-state PL spectra were recorded by a home-built optical setup using 457-, 488-, 532-, and 633-nm lasers for excitation. FTIR spectra were recorded by a Bruker Vertex 80v at room temperature in a continuous vacuum environment with typically 256 scans per loop and 4  $\text{cm}^{-1}$  resolution in the transmission and reflection mode. Raman scattering spectroscopy was performed using a micro-Raman spectrometer (Horiba-JY T64, 000) excited with a solid-state laser ( $\lambda = 514 \text{ nm}$ ) in the backscattering configuration. The backscattered signal was collected through a 100 $\times$  objective and dispersed by a 1,800- $\text{g}\cdot\text{mm}^{-1}$  grating; the laser power on the sample surface was measured to be approximately 1.0 mW.

The typical measurement time was 30 s. The XPS data were acquired using an Omicron EA125 analyzer with monochromatic Al K alpha ( $h\nu = 1,486.7$  eV) radiation. The room-temperature time-resolved PL spectra were obtained by a Becker-Hickl DCS-120 confocal scanning fluorescence lifetime imaging microscopy (FLIM) system, with excitation from a laser diode operating at 375 nm. The  $^1\text{H}$ NMR spectra of the oleylamine and Cdots were recorded by a Bruker BioSpin GmbH NMR300. To detect the feature peak of  $\text{sp}^2$  at 7.2 ppm, the Cdots were dispersed in  $\text{CD}_2\text{Cl}_2$ .

### 3 Results and discussion

#### 3.1 UV–Vis absorption and PL properties of Cdots

Figure 1(a) shows the UV–Vis absorption spectrum of Cdots synthesized by the pyrolysis of oleylamine with a reaction time of 10 min. The typical feature at  $\sim 230$  nm is attributed to the  $\pi-\pi^*$  transition of aromatic  $\text{sp}^2$  domains and the two absorption shoulders at  $\sim 275$  and  $\sim 300$  nm to the  $n-\pi^*$  transition [20]. The insets in Fig. 1(a) show the dispersion of Cdots with blue fluorescence under 254 nm UV light illumination.

Figure 1(b) presents the TEM image of the Cdots. The results reveal that the Cdots were mostly irregularly sphere with diameters in the range 4–13 nm. Their PL properties show an excitation-dependent behavior. The PL emission shifts to longer wavelengths and its intensity decreases with the increase of the excitation wavelength, which agrees with previous reports [1, 9, 17, 21]. The emission band maximum was 554, 560, 580, and 656 nm of the Cdots excited by 457-, 488-, 532-, and 633-nm lasers, respectively. The Cdots were dispersed in hexane and the laser power on the sample surface was measured to be approximately 80 mW. However, the PL intensity decreased drastically when the sample was excited with the 532- and 633-nm lasers. Until now, several mechanisms have been proposed to explain this excitation-dependent behavior, such as the presence of several different fluorophores within the carbogenic network [17] and a distribution of different emissive sites and sizes [10, 22]. However, the essence of the excitation-dependent behavior is debatable. Using our approach, other mercaptans, alkylamines, and silanes, such as octadecanethiol, dodecanethiol, HDTMSi, hexadecylamine, dodecylamine, APTMS, and AEPTMS, can

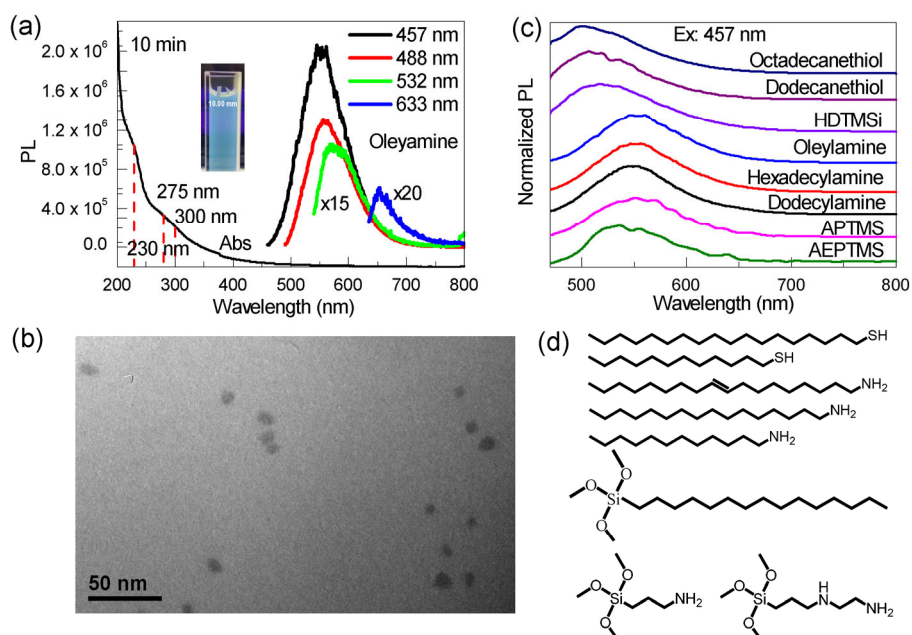


**Figure 1** (a) PL spectra of Cdots in hexane excited with different lasers and the corresponding absorption spectrum. The insets show the dispersion of Cdots with blue fluorescence under 254-nm UV light. (b) Typical TEM image of Cdots. (c) Normalized PL spectra of Cdots synthesized from other mercaptans, alkylamines, and silanes: octadecanethiol, dodecanethiol, HDTMSi, hexadecylamine, dodecylamine, APTMS, and AEPTMS. (d) The chemical structure of the mercaptans, alkylamines, and silanes.

also be used as sources to synthesize Cdots. Figure 1(c) shows the PL spectra of Cdots using different sources under excitation with a 457-nm laser. Figure 1(d) displays the chemical structure of those alkylamines and silanes.

### 3.2 Mechanism of the pyrolysis of oleylamine to Cdots

The basic procedures to synthesize Cdots include the decomposition and pyrolysis of oleylamine in air. FTIR spectroscopy and  $^1\text{H}$ NMR spectroscopy were used to confirm the reaction process. To eliminate the FTIR signal interference due to  $\text{H}_2\text{O}$  in the air, the Cdots were drop-casted on 50-nm-thick Au films to form thin films and then measured in a continuous vacuum environment in the reflection mode. The oleylamine liquid films were examined in a vacuum environment in the transmission mode. Figure 2(a) shows the FTIR spectra of the oleylamine and Cdots. The bands at 2,924 and 2,853  $\text{cm}^{-1}$  can be ascribed to the symmetric and asymmetric stretching vibrations of the C–H bonds from  $\text{CH}_2$  and  $\text{CH}_3$  [23–26]. The peaks at 1,467 and 1,378  $\text{cm}^{-1}$  can be assigned to the asymmetric in-plane and symmetric rocking mode of C–H [25]. The peaks at 1,306 and 1,073  $\text{cm}^{-1}$  in the oleylamine spectrum are attributed to the stretching vibrations of  $\text{CH}_2\text{--CH}_3$  and C–N. However, the direct FTIR analysis of the Cdots did not obtain detectable FTIR signals, indicating that  $\text{CH}_2\text{--CH}_3$  and C– $\text{NH}_2$  were carbonized. The peak of oleylamine at 722  $\text{cm}^{-1}$  corresponds to the in-plane rocking vibration of the  $\text{CH}_2$  bond from  $(\text{CH}_2)_n$  chains, where  $n > 4$  [24]. However, the fractions of the peak at 722  $\text{cm}^{-1}$  drastically decrease in Cdots, which indicates that the long chains of oleylamine are broken during carbonization. After carbonization, the stretching vibrations and in-plane rocking mode of N–H at 3,375, 1,571, and 796  $\text{cm}^{-1}$  and the C–N stretch peak of oleylamine at 1,073  $\text{cm}^{-1}$  disappear [27, 28], which indicates that the  $\text{--C--NH}_2$  groups of oleylamine are oxidized. It is important to note that a new band appears at 1,710 and 1,600  $\text{cm}^{-1}$ , which is assigned to the stretching vibrations of C=O and the ring stretching vibrations of the phenyl group, respectively. The oleylamine peaks at 3,005, 1,621, and 967  $\text{cm}^{-1}$  can be assigned to the stretching vibrations of =C–H and  $\text{--C=C--}$  and the

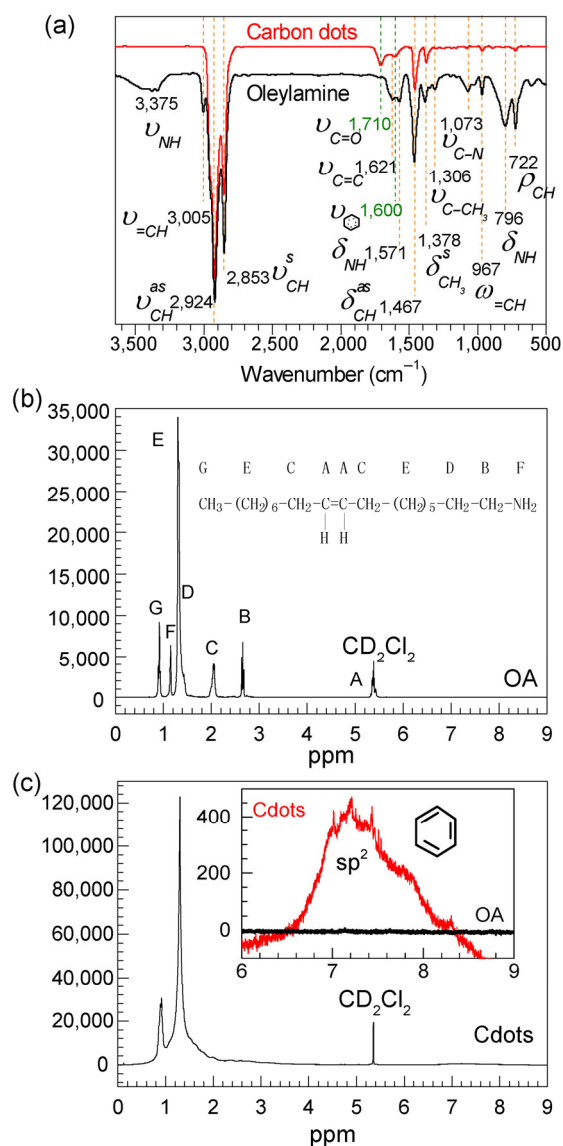


**Figure 2** (a) FTIR spectra of oleylamine and Cdots, (b) and (c)  $^1\text{H}$ NMR spectra of oleylamine and Cdots. The insets in (c) demonstrate the formation of  $\text{sp}^2$  clusters in Cdots.

out-of-plane rocking mode of =C–H [25]. However, the peaks at 3,005 and 1,621  $\text{cm}^{-1}$  disappear, which indicates that the  $\text{CH=CH}$  groups were broken and the left small peak at  $\sim 967$   $\text{cm}^{-1}$  is attributed to the C–O groups in Cdots. To further confirm the formation of  $\text{sp}^2$  clusters, the  $^1\text{H}$ NMR spectra of oleylamine and Cdots in  $\text{CD}_2\text{Cl}_2$  solvent were examined, as shown in Figs. 2(b) and 2(c). It is important to note that the  $^1\text{H}$ NMR feature peak of the phenyl group at  $\sim 7.2$  ppm was detected in Cdots. However, it was not observed in oleylamine. Therefore,  $\text{O}_2$  from air participated in the pyrolysis of oleylamine and  $\text{sp}^2$  clusters or

fragments were formed in the Cdots. Oleylamines are oxidized into carbon compounds consisting of  $sp^2$  clusters (phenyl group), C=O, C–O,  $-CH_2-$ , and  $-CH_3$  species.

Raman spectroscopy and XPS were further used to investigate the composition of Cdots. Figure 3(a) shows the Raman spectra of Cdots excited with a 514-nm laser. Two fingerprint features of carbon, the D band and G band, are clearly observed at 1,347 and 1,586  $cm^{-1}$ , respectively [29]. The D band is related to the presence of  $sp^3$  defects and the G band corresponds to the in-plane stretching vibration of  $sp^2$  carbon atoms, which is a doubly degenerate (TO and LO) phonon

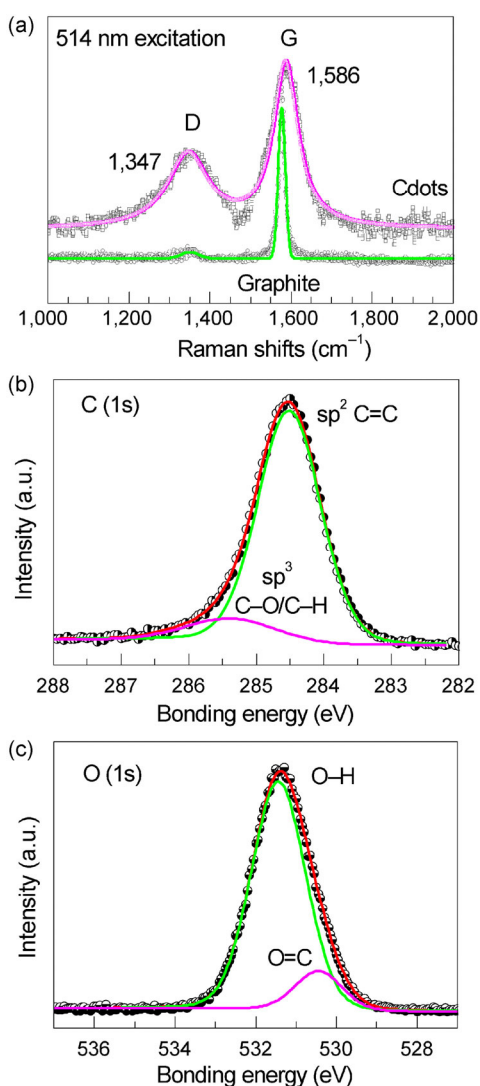


**Figure 3** (a) Raman spectra of Cdots and graphite excited with a 514-nm laser, (b) and (c) XPS spectra of Cdots. The solid lines represent a fit to the data.

mode ( $E_{2g}$  symmetry) at the center of the Brillouin zone [30, 31]. The increasing phenyl group units in the  $sp^2$  domain result in a blue shift of the G band [32]. The XPS Cdot data of C1s are shown in Fig. 3(b). The peaks at 284.5 and 285.4 eV are assigned to  $sp^2$  carbon (C=C) and  $sp^3$  carbon (C–O/C–H) clusters, respectively, in agreement with previous FTIR,  $^1H$ NMR, and Raman spectroscopy results [30, 33, 34]. As shown in the O1s XPS data, the peak at 530.5 eV contains contributions from C=O groups whereas the peak at 531.4 eV is assigned to C–O and O–C–O groups [35–37], which further verifies the FTIR results. It is important to note that the possible contribution from water molecules can be excluded based on four arguments: (1) The Cdots are hydrophobic and passivated with long-chain alkyl groups, (2) the sample was extracted by centrifugation and washing in THF, (3) the sample was heated at 100 °C and pumped before XPS was performed, (4) the FTIR data measured in vacuum do not show any feature peaks of water molecules. Therefore, the Raman and XPS data confirm that the Cdots contain a mixture of  $sp^2$  clusters and a few conjugated repeating units dispersed in an insulating  $sp^3$  matrix, in which a fraction of the carbons are bonded with oxygen (C=O, O=C–OH groups); this is consistent with the UV–Vis,  $^1H$ NMR, and FTIR results.

### 3.3 Aromatic $sp^2$ domains for the observed blue PL

To understand the PL mechanism, we synthesized Cdots using different reaction times and further investigated the time dependence of their absorption, PL, and lifetime. As shown in Fig. 4(a), the UV absorption peak of the  $\pi$ – $\pi^*$  transition of aromatic  $sp^2$  domains is red-shifted from 217 to 230 nm as the reaction time increases from 1 to 10 min and further shifted slightly to 232 nm at 30 min. Li et al. calculated the dependence of the HOMO–LUMO gap on the size of graphene fragments and suggested that the gap decreases gradually as the size of the fragment increases [8]. Eda et al. calculated the energy gap between the  $\pi$ – $\pi^*$  states, which decreases as the size of the  $sp^2$  clusters or conjugation length increases [19]. Therefore, we propose that small  $sp^2$  clusters or fragments of a few aromatic rings are responsible

for the observed blue PL of our Cdots, which were synthesized by the pyrolysis process. The red shift of the  $\pi$ - $\pi^*$  transition absorption peak is attributed to the increased size of the  $sp^2$  clusters. The broad absorption peak of the  $\pi$ - $\pi^*$  transition indicates that the size distribution of the  $sp^2$  cluster is inhomogeneous. The most obvious absorption peak line-shape at 5 min is probably due to the conjunction of  $sp^2$  domains and C=O and -CH<sub>3</sub> groups, consistent with previous works [38]. The absorption peaks of the  $n$ - $\pi^*$  transition at ~275 and 300 nm are attributed to the electronic transition of the C-OH and C=O groups, respectively. The FTIR and XPS data confirmed that the two groups, C-OH and C=O, are formed in the Cdots. The electronic orbital energy of the  $n$  state of the C-OH group is lower than that of the C=O group [39]. Therefore, the energy gap for the  $n$ - $\pi^*$  transition of the C-OH group is larger than that of the C=O group, resulting in a blue shift of the absorption peak.

Theoretically, the  $n$ - $\pi^*$  energy gap is independent of the size of the  $sp^2$  clusters. Therefore, the absorption peaks of the  $n$ - $\pi^*$  transition for our Cdots are not shifted as the reaction time increases from 1 to 30 min.

Figure 4(b) shows the normalized PL spectra of Cdots synthesized with different reaction times varying from 1 to 30 min, obtained using excitation by a 457-nm laser. It is clearly observed that the PL position is red-shifted from 544 to 553 nm when the reaction time increases from 1 to 30 min, which indicates that the energy gap between the  $\pi$ - $\pi^*$  states decreases, in

agreement with the absorption data. Therefore, the size of the  $sp^2$  clusters increases as the reaction time increases. All luminescent Cdots have a quantum efficiency of ~3%. It is important to note that the PL and absorbance measurement conditions for all Cdots were approximately the same, which ensured that the comparisons of the PL and absorbance absolute intensities are convincing. As shown from the absolute intensity PL spectra (the inset in Fig. 4(b)), the PL intensity monotonously increases to a maximum at 10 min and then decreases with increasing reaction time from 10 to 30 min. The absorption data in the inset in Fig. 4(a) show that the absorption intensity of the  $\pi$ - $\pi^*$  transition first increases, reaches a maximum at 20 min, and then drastically decreases at 30 min; this indicates that the concentration of luminescent  $sp^2$  clusters in the Cdots becomes maximum at ~20 min. Therefore, the observed increase in the PL intensity is attributed to the increased concentration of the strongly localized  $sp^2$  sites. Although the concentration of the  $sp^2$  sites at 20 min is larger than that at 10 min, the PL intensity at 20 min is smaller than at 10 min. Therefore, the subsequent PL intensity decrease at 20 min is due to the percolation between the  $sp^2$  configurations, which facilitates the transport of excitons to nonradiative recombination sites and thus leads to PL quenching [19]. With a longer reaction time, excessive carbonization occurs, which results in the drastically decreased concentration of luminescent Cdots. Therefore, the absorption and PL intensity drastically decrease.

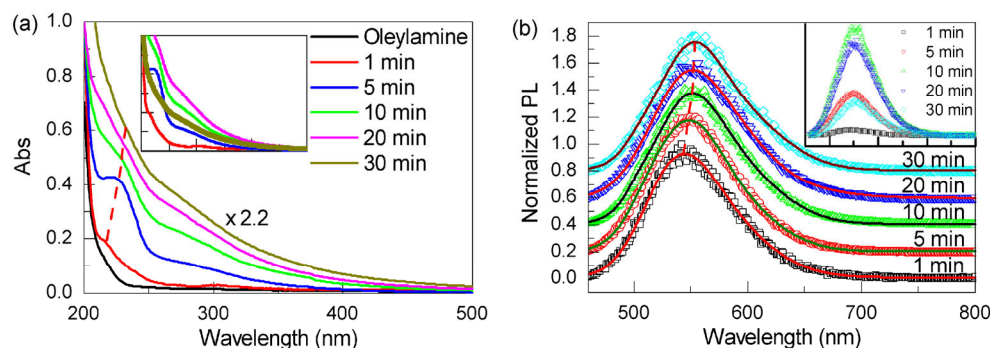


**Figure 4** (a) UV-Vis absorption spectra of oleylamine and Cdots at different reaction times between 1 and 30 min. To clearly show the red shift of the absorption peak, the absorption intensity of the Cdots at 30 min was multiplied by 2.2. The inset shows the original absorption intensity data. (b) Normalized PL spectra of Cdots excited with a 457-nm laser. The solid lines are fitting curves to the data using the Gaussian peak function. The inset displays the non-normalized PL spectra of the Cdots.

However, it is important to note that both the absorption and PL data clearly show that the size of the  $sp^2$  clusters increases with increasing reaction time. The absorption and PL intensity depend on the concentration of the formed  $sp^2$  clusters. However, a high concentration facilitates the percolation between  $sp^2$  clusters, leading to nonradiative energy transfer and thus PL quenching, which is similar to in the behavior of CdSe/ZnS quantum dot films [40].

### 3.4 Electron–hole exchange interaction

The time-resolved PL spectra of luminescent Cd dot drop-casted films were recorded by a confocal scanning fluorescence lifetime imaging microscopy system and are shown in Fig. 5(a) [41, 42]. The time-resolved PL decay curve is well fitted by the biexponential function,  $I(t) = A_1 \exp(-t/\tau_1) + A_2 \exp(-t/\tau_2)$ , with two time constants: a fast decay ( $\tau_1$ ), accompanied by a long-living emission ( $\tau_2$ ), where  $I(t)$  is the PL intensity [43, 44]. Because of the inhomogeneous

distribution of  $sp^2$  cluster lifetimes, the emission kinetics shows a multiexponential behavior distributed over a large time scale [45]. The lifetime of the long-lived decay component is assumed to correspond to the lifetime of the film samples [46], which was determined to be dependent on the reaction time. As the reaction time increases, the lifetime of the Cdots decreases. The fluorescence lifetimes  $\tau_1$  are  $1.2 \pm 0.06$ ,  $0.7 \pm 0.01$ ,  $0.5 \pm 0.01$ ,  $0.4 \pm 0.01$ , and  $0.3 \pm 0.01$  ns and the  $\tau_2$  ones are  $6.5 \pm 0.01$ ,  $3.9 \pm 0.02$ ,  $2.5 \pm 0.02$ ,  $1.9 \pm 0.02$ , and  $1.2 \pm 0.02$  ns for the reaction times 1, 5, 10, 20, and 30 min, respectively. The absorption and PL data of the Cdots show that the size of the  $sp^2$  clusters increases with increasing reaction time. Therefore, we propose that an electron–hole exchange interaction occurs in the luminescent Cdots, leading to the splitting of the excitonic states and thus the size dependence of their lifetimes, which is consistent with previous reports [46, 47]. Donegá et al. [48] and Brongersma et al. [49] investigated the size dependence of the band-

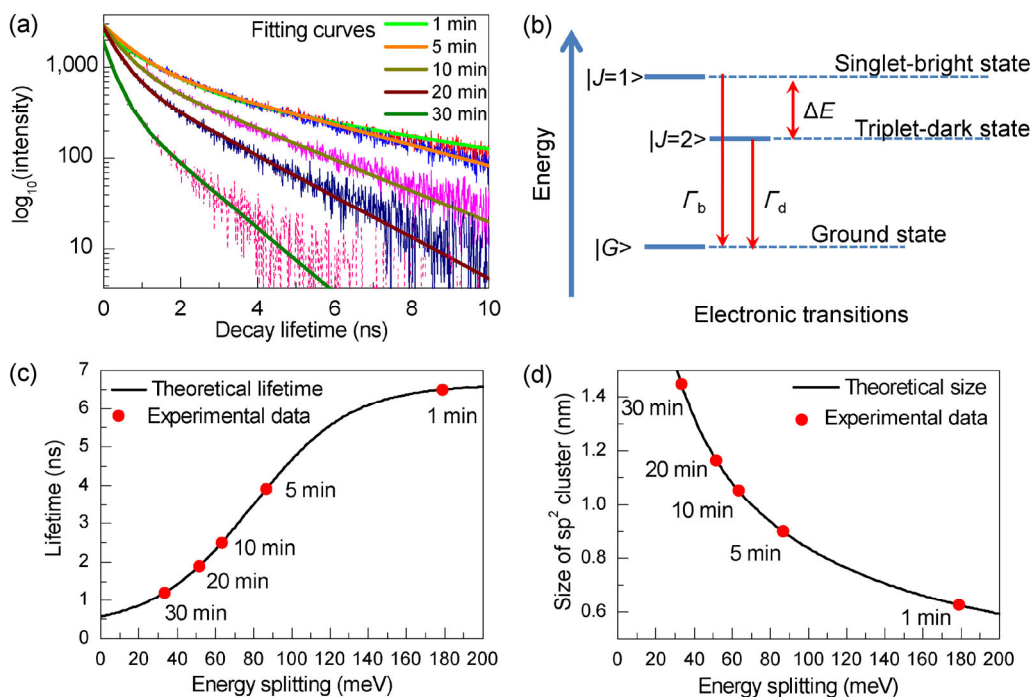


**Figure 5** (a) Time-resolved PL spectra of Cdots synthesized using different reaction times. The lifetime decreases as the reaction time increases. The solid lines are fitting curves to the data using a biexponential function. (b) Schematic diagram of a three-level model with the singlet-bright, triplet-dark, and ground states. (c) Lifetime as a function of the energy splitting between the singlet-bright and triplet-dark states ( $\Delta E$ ). The red solid circles are the experimental long-living emission lifetime, extracted from (a), and the black solid line is a fit to the data using Eq. (2), as described in the text. (d) Size of  $sp^2$  clusters ( $d$ ) vs. energy splitting ( $\Delta E$ ). The red solid circles denote the energy splitting extracted from (c) and the black solid curve is a fit to the data using Eq. (3).

edge PL decay of CdSe quantum dots with diameters ranging from 1.7 to 6.3 nm and Si nanocrystals with diameters in the range of 2 to 5.5 nm. Both works were based on a three-level system consisting of a zero-exciton ground level and excitonic singlet and triplet states. These studies demonstrated that the lifetime decreases with increasing quantum-dot size owing to the decreased electron–hole exchange interaction, which results in the decrease of the energy gap between the excitonic singlet and triplet states. For the electronic states of the graphene structure, 16 exciton states have been proposed that originate from the spin and degeneracy of band structures in the  $K$  and  $K'$  valleys in the momentum space. However, the optical transition from only one exciton state to the ground state is dipole allowed and is defined as the singlet-bright exciton state. The other 15 exciton states are optically forbidden and are defined as triplet-dark exciton states [47]. Therefore, the exciton states of the  $sp^2$  clusters can be classified into singlet and triplet states of the electron–hole spin configuration. Figure 5(b) shows a schematic of a three-level model with singlet-bright ( $J = 1$ ) and triplet-dark ( $J = 2$ ) excitonic states and a zero-exciton ground state (G). The dark state lies below the bright state with an energy splitting  $\Delta E$ .  $\Gamma_b$  and  $\Gamma_d$  are the radiative rates from the singlet-bright ( $J = 1$ ) and the triplet-dark ( $J = 2$ ) states to the ground state (G), respectively. The  $|J = 1\rangle \rightarrow |J = 2\rangle$  and  $|J = 2\rangle \rightarrow |J = 1\rangle$  rates are, respectively,  $\gamma_b = \gamma_0(N_B + 1)$  and  $\gamma_d = \gamma_0 N_B$ , where  $N_B = [\exp(\Delta E/k_B T) - 1]^{-1}$  is the Bose-Einstein phonon number at temperature  $T$ ,  $\gamma_0$  is the relaxation rate of the  $|J = 1\rangle \rightarrow |J = 2\rangle$  transition at zero temperature [45], and  $\gamma_b n_b = \gamma_d n_d$ , where  $n_b$  and  $n_d$  are the numbers of excitons at the singlet-bright and triplet-dark states, respectively. Therefore, we can obtain  $n_b \exp(\Delta E/k_B T) = n_d$ . By defining  $N = n_b + n_d$  as the total number of excitons, the decay rate ( $\Gamma$ ) of the excitons is given by [46, 50]

$$-\frac{dN}{dt} = n_b \Gamma_b + n_d \Gamma_d \quad (1)$$

$$\Gamma = \frac{1}{\tau} = \frac{\Gamma_b + \Gamma_d e^{\Delta E/k_B T}}{1 + e^{\Delta E/k_B T}} \quad (2)$$

where  $\tau$  is the lifetime and  $k_B$  is the Boltzmann constant,  $8.617 \times 10^{-5} \text{ eV}\cdot\text{K}^{-1}$ . The temperature  $T$  was 298 K

in our experiments. Using Eq. (2), the experimental long-living emission lifetime data were fitted, as shown in Fig. 5(c). As the lifetime increases,  $\Delta E$  increases. The calculated energy splitting  $\Delta E$  was 179, 86.6, 63.3, 51.7, and 33.4 meV, respectively, for reaction times 1, 5, 10, 20, and 30 min. Previous reports have shown that the energy splitting  $\Delta E$  and the exciton lifetime increase with decreasing size of luminescent nanoparticles [45, 47, 49]. Brovelli et al. investigated the strong electron–hole exchange interaction in CdSe/CdS core–shell semiconductor nanocrystals and demonstrated that the relationship between the bright–dark energy splitting and the nanocrystal size can be fitted by the equation  $70/d_1^2$  meV, where  $d_1$  is the diameter of the nanocrystals in nanometers [46]. Matsunaga et al. determined the tube-diameter dependence of the energy splitting for carbon nanotubes,  $\Delta E = 70/d_2^2$  (meV), where  $d_2$  is the diameter of the carbon nanotubes in nanometers [51]. Therefore, the size of the  $sp^2$  clusters,  $d$ , is defined as

$$d = \sqrt{70 / \Delta E} \quad (3)$$

where the units of  $d$  and  $\Delta E$  are nanometers and millielectronvolts, respectively. Figure 5(d) shows the fitting curve. The size of the  $sp^2$  clusters increases with the decrease of the energy splitting. The  $sp^2$  cluster size is 0.6, 0.9, 1.1, 1.2, and 1.4 nm for reaction time 1, 5, 10, 20, and 30 min, respectively, which is in good agreement with the absorption and PL data. The decrease of the  $sp^2$  cluster size produces an increasing confinement energy and a stronger electron–hole exchange interaction [48]. Therefore, the energy splitting  $\Delta E$  increases, resulting in an increased lifetime.

## 4 Conclusions

In summary, luminescent Cdots have been synthesized by the simple one-step method of the pyrolysis of oleylamine, which is the only involved chemical, acting simultaneously as a solvent, a precursor, and a passivation agent in the synthetic system. FTIR data showed that oleylamines are oxidized into carbon compounds, including (C=C) $_n$ , C–O, O–H, and C–H species.  $^1\text{H}$ NMR, Raman, and XPS data confirmed

that the  $sp^2$  clusters are formed and dispersed in an insulating  $sp^3$  matrix. The absorption peaks of the  $\pi-\pi^*$  transition and PL peaks of the Cdots are red-shifted as the reaction time increases. Therefore, the  $sp^2$  clusters are responsible for the observed blue PL and the  $sp^2$  cluster size increases with increasing reaction time. The exciton states of the  $sp^2$  clusters are classified into singlet-bright and triplet-dark states. The bright-dark energy splitting decreases as the  $sp^2$  cluster size increases, as a result of the decreasing confinement energy and weaker electron-hole exchange interaction, which results in the decreased decay lifetime of the Cdots.

## Acknowledgements

Q. H. X. gratefully thanks the strong support from Singapore National Research Foundation through a Competitive Research Program (No. NRF-CRP-6-2010-2), and Singapore Ministry of Education via two Tier2 grants (Nos. MOE2011-T2-2-051 and MOE2011-T2-2-085) and a Tier1 grant (No. 2013-T1-002-232).

## References

- [1] Baker, S. N.; Baker, G. A. Luminescent carbon nanodots: Emergent nanolights. *Angew. Chem., Int. Ed.* **2010**, *49*, 6726–6744.
- [2] Li, H. T.; Kang, Z. H.; Liu, Y.; Lee, S. T. Carbon nanodots: Synthesis, properties and applications. *J. Mater. Chem.* **2012**, *22*, 24230–24253.
- [3] Pan, J.; Utama, M. I. B.; Zhang, Q.; Liu, X. F.; Peng, B.; Wong, L. M.; Sum, T. C.; Wang, S. J.; Xiong, Q. H. Composition-tunable vertically aligned  $CdS_xSe_{1-x}$  nanowire arrays via van der waals epitaxy: Investigation of optical properties and photocatalytic behavior. *Adv. Mater.* **2012**, *24*, 4151–4156.
- [4] Loh, K. P.; Bao, Q. L.; Eda, G.; Chhowalla, M. Graphene oxide as a chemically tunable platform for optical applications. *Nat. Chem.* **2010**, *2*, 1015–1024.
- [5] Wang, J.; Wang, C. F.; Chen, S. Amphiphilic egg-derived carbon dots: Rapid plasma fabrication, pyrolysis process, and multicolor printing patterns. *Angew. Chem., Int. Ed.* **2012**, *51*, 9297–9301.
- [6] Xu, X. Y.; Ray, R.; Gu, Y. L.; Ploehn, H. J.; Gearheart, L.; Raker, K.; Scrivens, W. A. Electrophoretic analysis and purification of fluorescent single-walled carbon nanotube fragments. *J. Am. Chem. Soc.* **2004**, *126*, 12736–12737.
- [7] Zhang, W. F.; Zhu, H.; Yu, S. F.; Yang, H. Y. Observation of lasing emission from carbon nanodots in organic solvents. *Adv. Mater.* **2012**, *24*, 2263–2267.
- [8] Li, H. T.; He, X. D.; Kang, Z. H.; Huang, H.; Liu, Y.; Liu, J. L.; Lian, S. Y.; Tsang, C. H. A.; Yang, X. B.; Lee, S.-T. Water-soluble fluorescent carbon quantum dots and photocatalyst design. *Angew. Chem., Int. Ed.* **2010**, *49*, 4430–4434.
- [9] Pan, D. Y.; Zhang, J. C.; Li, Z.; Wu, M. H. Hydrothermal route for cutting graphene sheets into blue-luminescent graphene quantum dots. *Adv. Mater.* **2010**, *22*, 734–738.
- [10] Liu, H. P.; Ye, T.; Mao, C. D. Fluorescent carbon nanoparticles derived from candle soot. *Angew. Chem., Int. Ed.* **2007**, *46*, 6473–6475.
- [11] Tian, L.; Ghosh, D.; Chen, W.; Pradhan, S.; Chang, X. J.; Chen, S. W. Nanosized carbon particles from natural gas soot. *Chem. Mater.* **2009**, *21*, 2803–2809.
- [12] Wang, X. H.; Qu, K. G.; Xu, B. L.; Ren, J. S.; Qu, X. G. Microwave assisted one-step green synthesis of cell-permeable multicolor photoluminescent carbon dots without surface passivation reagents. *J. Mater. Chem.* **2011**, *21*, 2445–2450.
- [13] Pan, D. Y.; Zhang, J. C.; Li, Z.; Wu, C.; Yan, X. M.; Wu, M. H. Observation of pH-, solvent-, spin-, and excitation-dependent blue photoluminescence from carbon nanoparticles. *Chem. Commun.* **2010**, *46*, 3681–3683.
- [14] Xie, Z.; Wang, F.; Liu, C. Y. Organic-inorganic hybrid functional carbon dot gel glasses. *Adv. Mater.* **2012**, *24*, 1716–1721.
- [15] Wang, F.; Pang, S. P.; Wang, L.; Li, Q.; Kreiter, M.; Liu, C. Y. One-step synthesis of highly luminescent carbon dots in noncoordinating solvents. *Chem. Mater.* **2010**, *22*, 4528–4530.
- [16] Ju, S.-Y.; Kopcha, W. P.; Papadimitrakopoulos, F. Brightly fluorescent single-walled carbon nanotubes via an oxygen-excluding surfactant organization. *Science* **2009**, *323*, 1319–1323.
- [17] Bourlino, A. B.; Stassinopoulos, A.; Anglos, D.; Zboril, R.; Karakassides, M.; Giannelis, E. P. Surface functionalized carbogenic quantum dots. *Small* **2008**, *4*, 455–458.
- [18] Zhou, J. G.; Booker, C.; Li, R. Y.; Zhou, X. T.; Sham, T.-K.; Sun, X. L.; Ding, Z. F. An electrochemical avenue to blue luminescent nanocrystals from multiwalled carbon nanotubes (MWCNTs). *J. Am. Chem. Soc.* **2007**, *129*, 744–745.
- [19] Eda, G.; Lin, Y. Y.; Mattevi, C.; Yamaguchi, H.; Chen, H. A.; Chen, I. S.; Chen, C. W.; Chhowalla, M. Blue photoluminescence from chemically derived graphene oxide. *Adv. Mater.* **2010**, *22*, 505–509.
- [20] Luo, Z. T.; Lu, Y.; Somers, L. A.; Johnson, A. T. C. High yield preparation of macroscopic graphene oxide membranes. *J. Am. Chem. Soc.* **2009**, *131*, 898–899.

- [21] Wang, F.; Xie, Z.; Zhang, H.; Liu, C. Y.; Zhang, Y. G. Highly luminescent organosilane-functionalized carbon dots. *Adv. Funct. Mater.* **2011**, *21*, 1027–1031.
- [22] Sun, Y. P.; Zhou, B.; Lin, Y.; Wang, W.; Fernando, K. A. S.; Pathak, P.; Mezziani, M. J.; Harruff, B. A.; Wang, X.; Wang, H. F. et al. Quantum-sized carbon dots for bright and colorful photoluminescence. *J. Am. Chem. Soc.* **2006**, *128*, 7756–7757.
- [23] Wu, H. B.; Chen, W. Synthesis and reaction temperature-tailored self-assembly of copper sulfide nanoplates. *Nanoscale* **2011**, *3*, 5096–5102.
- [24] Cattley, C. A.; Stavrinadis, A.; Beal, R.; Moghal, J.; Cook, A. G.; Grant, P. S.; Smith, J. M.; Assender, H.; Watt, A. A. R. Colloidal synthesis of lead oxide nanocrystals for photovoltaics. *Chem. Commun.* **2010**, *46*, 2802–2804.
- [25] Hou, X. M.; Zhang, X. L.; Yang, W.; Liu, Y.; Zhai, X. M. Synthesis of SERS active Ag<sub>2</sub>S nanocrystals using oleylamine as solvent, reducing agent and stabilizer. *Mater. Res. Bull.* **2012**, *47*, 2579–2583.
- [26] Hu, S.-L.; Niu, K.-Y.; Sun, J.; Yang, J.; Zhao, N.-Q.; Du, X.-W. One-step synthesis of fluorescent carbon nanoparticles by laser irradiation. *J. Mater. Chem.* **2009**, *19*, 484–488.
- [27] Kisner, A. *Ultrathin Gold Nanowires: Chemistry, Electrical Characterization and Application to Sense Cellular Biology*; Forschungszentrum Jülich, Zentralbibliothek: Jülich, 2012.
- [28] Gericke, A.; Hühnerfuss, H. Infrared spectroscopic comparison of enantiomeric and racemic N-octadecanoylserine methyl ester monolayers at the air/water interface. *Langmuir* **1994**, *10*, 3782–3786.
- [29] Wang, Y.; Alsmeyer, D. C.; McCreery, R. L. Raman spectroscopy of carbon materials: Structural basis of observed spectra. *Chem. Mater.* **1990**, *2*, 557–563.
- [30] Lu, J.; Yang, J. X.; Wang, J. Z.; Lim, A. L.; Wang, S.; Loh, K. P. One-pot synthesis of fluorescent carbon nanoribbons, nanoparticles, and graphene by the exfoliation of graphite in ionic liquids. *ACS Nano* **2009**, *3*, 2367–2375.
- [31] Ray, S. C.; Saha, A.; Jana, N. R.; Sarkar, R. Fluorescent carbon nanoparticles: Synthesis, characterization, and bioimaging application. *J. Phys. Chem. C.* **2009**, *113*, 18546–18551.
- [32] Tommasini, M.; Castiglioni, C.; Zerbi, G. Raman scattering of molecular graphenes. *Phys. Chem. Chem. Phys.* **2009**, *11*, 10185–10194.
- [33] Haerle, R.; Riedo, E.; Pasquarello, A.; Baldereschi, A. sp<sup>2</sup>/sp<sup>3</sup> hybridization ratio in amorphous carbon from C 1s core-level shifts: X-ray photoelectron spectroscopy and first-principles calculation. *Phys. Rev. B* **2001**, *65*, 045101.
- [34] Yumitori, S. Correlation of C1s chemical state intensities with the O1s intensity in the XPS analysis of anodically oxidized glass-like carbon samples. *J. Mater. Sci.* **2000**, *35*, 139–146.
- [35] Yu, X. L.; Tong, S. R.; Ge, M. F.; Wu, L. Y.; Zuo, J. C.; Cao, C. Y.; Song, W. G. Adsorption of heavy metal ions from aqueous solution by carboxylated cellulose nanocrystals. *J. Environ. Sci.* **2013**, *25*, 933–943.
- [36] Yang, D. X.; Velamakanni, A.; Bozoklu, G.; Park, S.; Stoller, M.; Piner, R. D.; Stankovich, S.; Jung, I.; Field, D. A.; Ventrice, C. A. Jr. et al. Chemical analysis of graphene oxide films after heat and chemical treatments by X-ray photoelectron and micro-Raman spectroscopy. *Carbon* **2009**, *47*, 145–152.
- [37] Chen, J. P.; Yang, L. Study of a heavy metal biosorption onto raw and chemically modified *Sargassum* sp. via spectroscopic and modeling analysis. *Langmuir* **2006**, *22*, 8906–8914.
- [38] Sk, M. P.; Jaiswal, A.; Paul, A.; Ghosh, S. S.; Chattopadhyay, A. Presence of amorphous carbon nanoparticles in food caramels. *Sci. Rep.* **2012**, *2*, 383.
- [39] Taylor, P. R. On the origins of the blue shift of the carbonyl n–π\* transition in hydrogen-bonding solvents. *J. Am. Chem. Soc.* **1982**, *104*, 5248–5249.
- [40] Nizamoglu, S.; Demir, H. V. Excitation resolved color conversion of CdSe/ZnS core/shell quantum dot solids for hybrid white light emitting diodes. *J. Appl. Phys.* **2009**, *105*, 083112.
- [41] Peng, B.; Li, Z. P.; Mutlugun, E.; Hernández Martínez, P. L.; Li, D. H.; Zhang, Q.; Gao, Y.; Demir, H. V.; Xiong, Q. H. Quantum dots on vertically aligned gold nanorod monolayer: Plasmon enhanced fluorescence. *Nanoscale* **2014**, *6*, 5592–5598.
- [42] Peng, B.; Li, G. Y.; Li, D. H.; Dodson, S.; Zhang, Q.; Zhang, J.; Lee, Y. H.; Demir, H. V.; Ling, X. Y.; Xiong, Q. H. Vertically aligned gold nanorod monolayer on arbitrary substrates: Self-assembly and femtomolar detection of food contaminants. *ACS Nano* **2013**, *7*, 5993–6000.
- [43] Peng, B.; Zhang, Q.; Liu, X. F.; Ji, Y.; Demir, H. V.; Huan, C. H. A.; Sum, T. C.; Xiong, Q. H. Fluorophore-doped core-multishell spherical plasmonic nanocavities: Resonant energy transfer toward a loss compensation. *ACS Nano* **2012**, *6*, 6250–6259.
- [44] Zhang, Q.; Liu, X. F.; Utama, M. I. B.; Zhang, J.; de la Mata, M.; Arbiol, J.; Lu, Y. H.; Sum, T. C.; Xiong, Q. H. Highly enhanced exciton recombination rate by strong electron–phonon coupling in single ZnTe nanobelt. *Nano Lett.* **2012**, *12*, 6420–6427.
- [45] Labeau, O.; Tamarat, P.; Lounis, B. Temperature dependence of the luminescence lifetime of single CdSe/ZnS quantum dots. *Phys. Rev. Lett.* **2003**, *90*, 257404.

- [46] Brovelli, S.; Schaller, R. D.; Crooker, S. A.; García-Santamaría, F.; Chen, Y.; Viswanatha, R.; Hollingsworth, J. A.; Htoon, H.; Klimov, V. I. Nano-engineered electron–hole exchange interaction controls exciton dynamics in core–shell semiconductor nanocrystals. *Nat. Commun.* **2011**, *2*, 280.
- [47] Matsuda, K. Novel excitonic properties of carbon nanotube studied by advanced optical spectroscopy. In *Progress in Nanophotonics 2*; Ohtsu, M., Ed.; Springer: Berlin Heidelberg, 2013; pp 33–70.
- [48] de Mello Donegá, C.; Bode, M.; Meijerink, A. Size- and temperature-dependence of exciton lifetimes in CdSe quantum dots. *Phys. Rev. B* **2006**, *74*, 085320.
- [49] Brongersma, M. L.; Kik, P. G.; Polman, A.; Min, K. S.; Atwater, H. A. Size-dependent electron–hole exchange interaction in Si nanocrystals. *Appl. Phys. Lett.* **2000**, *76*, 351–353.
- [50] Crooker, S. A.; Barrick, T.; Hollingsworth, J. A.; Klimov, V. I. Multiple temperature regimes of radiative decay in CdSe nanocrystal quantum dots: Intrinsic limits to the dark-exciton lifetime. *Appl. Phys. Lett.* **2003**, *82*, 2793–2795.
- [51] Matsunaga, R.; Matsuda, K.; Kanemitsu, Y. Observation of charged excitons in hole-doped carbon nanotubes using photoluminescence and absorption spectroscopy. *Phys. Rev. Lett.* **2011**, *106*, 037404.